Development of multifunctional nanopipettes for controlled intracellular delivery and single-entity detection

Journal:	*Faraday Discussions*
Manuscript ID	FD-ART-08-2021-000057.R1
Article Type:	Paper
Date Submitted by the Author:	13-Sep-2021
Complete List of Authors:	Pandey, Popular; Florida International University, Physics Sesena Rubfiaro, Alberto; Florida International University, Physics department Khatri, Santosh; Florida International University, Physics department He, Jin; Florida International University, Physics department

ARTICLE

Development of Multifunctional Nanopipettes for Controlled Intracellular Delivery and Single-Entity Detection

Popular Pandey[a], Alberto Sesena-Rubfiaro[a], Santosh Khatri[a], Jin He[a, b]*

Received 00th January 20xx,
Accepted 00th January 20xx

DOI: 10.1039/x0xx00000x

Intracellular delivery of biomolecules and nanoscale materials to individual cells has gained remarkable attention in recent years owing to its wide applications in drug delivery, clinical diagnostics, bio-imaging, and single-cell analysis. It remains a challenge to control and measure the delivered amount in one cell. In this work, we developed a multifunctional nanopipette-containing both nanopore and nanoelectrode (pyrolytic carbon) at the apex- as a facile, minimal-invasive, and effective platform for both controllable single-cell intracellular delivery and single-entity counting. While controlled by a micromanipulator, the baseline changes of nanopore ionic current (I) and nanoelectrode open circuit potential (V) help to guide the nanopipette tip insertion and positioning processes. The delivery from the nanopore barrel can be facilely controlled by the applied nanopore bias. To optimize the intracellular single-entity detection while delivery, we studied the effects of nanopipette tip geometry and solution salt concentration in controlled experiments. We have successfully delivered gold nanoparticles and biomolecules into the cell, as confirmed by the increased scattering and fluorescence signals, respectively. The delivered entities have also been detected at the single-entity level by using either one or both transient I and V signals. We found the sensitivity of the single-entity electrochemical measurement was greatly affected by the local environment of the cell and varied between cell lines.

Keywords: Nanopore; nanoelectrode; nanopipette; single-cell analysis; single-entity electrochemistry; intracellular delivery

Introduction

Controlled cell manipulation and interrogation via localized intracellular delivery of biomolecules are becoming game-changing approaches to understand molecular biology at the single-cell level, manipulate cell function, reprogram cell behavior and treat diseases.[1, 2] Controlled delivery of functional nano-entities such as synthetic nanoparticles and nanostructures, RNA, plasmid DNA, proteins, and peptides into living cells have many applications ranging from gene expression and regulation, bio-imaging, cell based-therapies, drug delivery, tissue engineering, and wound healing.[2-12] In the last two decades, various delivery techniques have been developed.[4, 13] The most common techniques are viral and chemical transfections at the bulk cell level. The viral transfection is reliable with high efficiency but is expensive and limited to gene delivery.[14] Chemical transfection techniques in general have lower transfection efficiency with problems of endosomal entrapment and the degradation of the transfected entities.[4] Both techniques lack control of dosage and cannot deliver genes at a single cell.

Physical delivery approaches such as microinjection, electroporation,[15] fluidic force microscopy, carbon nanotube endoscope, nanostraw, nanowires, and nanoinjection have been introduced to achieve intracellular delivery.[4, 16] These techniques can deliver a wide range of exogenous materials to a wide range of cell lines. They are normally of low throughput but can deliver to individual cells and enable single-cell studies.[17-19] Glass or quartz micropipettes are commonly used for pressure-controlled microinjection. However, the microinjection also induces low cell viability due to the large tip diameters from 0.5 to 5 µm.[20-22] In recent years, various electroporation methods, such as nanofountain probe, nanostraw, flow-through electroporation, microchips electroporation, Fluidic force microscopy, and 2D nanopore-based electroporation platform, have been developed for intracellular delivery.[23-34] However, they also suffer problems of irreversible damage to the cell membrane and cell death due to high electric field, expensive device fabrication and poor dosage control during delivery.[29, 35-37] Carbon nanotube endoscopes and fluidic force microscopes have also been used for pressure-controlled cellular delivery.[38-42] These platforms have high cell viability post-injection however suffer limitations such as expensive device fabrication, and the requirement of the specialized probe.

Recently, nanopipettes with pore diameters below 300 nm have been utilized for single-cell delivery.[43-47] Different from other nanoscale delivery devices such as nanostraws and nanowires, nanopipettes can be easily fabricated from quartz/glass capillaries using pipette pullers. The reduction of the nanopipette tip size greatly improves the cell viability after injection.[21, 38] The nanopipette delivery can also be controlled

---

[a] Physics Department, Florida International University, Miami, Florida, 33199, USA
[b] Biomolecular Sciences Institute, Florida International University, Miami, Florida, 33199, USA

by the voltage which enables quick, facile, and precise control of delivered entities.[21, 43, 44] Pourmand's group have demonstrated the voltage-driven delivery system using single/double barrel nanopipettes via a scanning ion conductance microscope.[43] Mirkin's group have used the SECM platform as a high precision micromanipulator for volume-controlled intracellular delivery via a nanopipette.[47] Metal coated nanopipette was also used as an electrowetting nanoinjector with controlled dosage delivery and high transfection efficiency.[48]

Accurate assessment and control of delivery dosage is the main challenge in single-cell transfection. Currently, Fluorescence intensity, injection volume, and injection duration-based approaches have been widely used in an attempt for quantifying delivered entities.[35, 36, 48, 49] However, these approaches are unable to quantify the delivered number of molecules with high precision. Quantification of delivered entities at the single-molecule level has been achieved during delivery via nanopore devices.[49, 50] Timp group utilized silicon nitride nanopore for quantitative intracellular delivery of DNA plasmids via electroporation.[51] Angelis group implemented a 3D hollow nanoelectrode-based system to detect translocation signals during the delivery of gold nanorods into cells.[52] While both works demonstrate the capability of nanopore as a quantitative delivery platform, both approaches demand expensive nanofabrication steps and often require high threshold voltage to deliver entities.

Because of the rapid developments of nanopipette-based single-entity electrochemistry (SEE) measurement techniques,[45] we are interested to achieve the nanopipette-based intracellular delivery and SEE detection at the same time. Here we developed a multifunctional nanopipette-based intracellular delivery method that allows for SEE detecting of delivered molecules and monitoring the delivery process. The multifunctional nanopipette consists of a nanopore and a carbon nanoelectrode (CNE) at the apex of a nanopipette.[53] We first investigated and optimized the conditions to achieve intracellular SEE detection using both the nanopore based ionic current detection and CNE based open-circuit-potential (OCP) detection during the voltage-controlled intracellular delivery of various nanoentities. Recent studies have suggested the molecular crowding effect can be a beneficial factor for nanopore sensing.[54, 55] Indeed, we found the SEE detection inside the cell not only can be realized but often improved. We also found the *in situ* SEE detection is very useful in monitoring the delivery rate and the dissipation of delivered entities, and probing the local cellular environment.

Experimental Methods

Materials. FITC dye was purchased from Sigma-Aldrich. Thiol-PEG 5k (MW-5000, purity >95%) for 40 nm gold nanoparticles (GNPs) surface modification was purchased from Nanocs. The citrate stabilized 40 nm GNPs were bought from Ted Pella, Inc. Other chemicals in ACS grade were purchased from Fisher Scientific. The purchased chemicals were used without further purification. 130 mM PBS was prepared by diluting the 1X PBS in DI water. The anion concentration of the final solution was 0.13 M and has ionic strength of 0.147 M. The intracellular solution was prepared with the following composition: NaCl 8 mM, KCl 132.5 mM, MgCl$_2$ 2 mM, HEPES 10 mM, 7.2 pH adjusted with NaOH. The extracellular solution contained: NaCl 130 mM, KCl 3 mM, CaCl$_2$ 2 mM, MgCl$_2$ 1.2 mM, HEPES 10 mM, Glucose 5mM 7.4 pH adjusted with NaOH. Tyrode solution was prepared with: NaCl 140 mM, KCl 5 mM, CaCl$_2$ 1.8 mM, MgCl$_2$ 1 mM, HEPES 5 mM, NaH$_2$PO$_4$ 1mM, Glucose 10mM, 7.4 pH adjusted with NaOH. FITC stock solution was prepared in DMSO. The 20 µM FITC solution was prepared by diluting the stock solution in intracellular medium which contains only 0.2% DMSO. All solutions were prepared using deionized water (~18 MΩ) from a water purification system (Ultra Purelab system, ELGA/Siemens).

Quartz Nanopipette Fabrication. The fabrication of multifunctional nanopipettes from the quartz theta capillary tubes (FG-G QT120−90−7.5, Sutter Instrument) has been described in detail previously.[53] In brief, the dual-barrel nanopipettes were fabricated from the cleaned capillary tubes by using a laser pipette puller (P-2000, Sutter Instrument) with following parameters: HEAT = 825, FIL = 3, VEL = 40, DEL = 220, PUL = 190. Then one barrel is filled with pyrolytic carbon to form a CNE at the tip.[53] Single barrel quartz nanopipette was also fabricated from cleaned capillary tubes (QF-100-50-7.5, Sutter Instrument) with the following pipette puller parameters: HEAT = 795, FIL = 3, VEL = 40, DEL = 145, PUL = 180. The optical microscope, current-voltage (I-V) measurements and/or cyclic voltammetry (CV), and scanning electron microscope (SEM, JEOL JSM 6335F) were used to characterize the fabricated nanopipettes.

For the delivery experiments, the nanopore barrel was backfilled with nanoscale entities (molecules or GNPs) suspended in 130 mM PBS solution (for bath delivery) or in intracellular solution (for intracellular delivery). Then the nanopipette was centrifuged at 2000 rpm for 2 min. All intracellular delivery experiments were performed in an extracellular medium. The loaded nanopipette tip was imaged by dark-field microscope for the GNPs and fluorescence microscope for the fluorescent entities to evaluate the filling before the delivery experiments.

Preparation of PEGylated GNPs. The PEGylated GNPs were prepared by using a previously reported method[56] with small modifications. In brief, 6 μL of aqueous 10 mM thiol-PEG 5k was added to 1 mL of 40 nm citrate-coated GNPs (150 pM stock concentration), producing a molar ratio of thiol-PEG to GNPs of 105:1. The mixture was incubated overnight at room temperature to achieve full replacement of citrate ligands by thiol-PEG on the GNP surface. The mixture was then purified by centrifugation twice, each at 7000 *rpm* for 10 min. The supernatant was removed, and the pellet was re-suspended in 1 mL DI water. The prepared PEGylated GNPs were re-suspended in the intracellular medium or PBS solution. The PEG modification and the stability of the PEGylated GNPs in the intracellular medium or PBS solution are confirmed via UV-Vis spectroscopy.

Electrical Measurements. The current−time (i−t) and potential−time (V−t) traces are recorded using the experimental setups as illustrated in Figures 1a and 3a. We used freshly prepared Ag/AgCl wire electrodes and an Axopatch 200B amplifier (Molecular Devices Inc., CA) in voltage-clamp mode to measure the ionic current through the nanopore. A battery-powered high-input impedance differential amplifier was used to measure the local potential of the CNE. The bandwidth of the low-pass filter was 5 kHz for current. The data were recorded with a sampling rate of 50 kHz by using Digidata 1440A and software Axoscope 10.5 (Molecular Devices).

HEK293 cell culture. The HEK293H cell line was obtained from ThermoFisher Scientific Invitrogen (Waltham, MA) and cultured as previously described.[57] Briefly, HEK293H was maintained with DMEM/High Glucose medium (Corning, 10-013-CV) supplemented with fetal bovine serum 10% (Gibco, 16140-071) and 1% Pen Strep (Gibco, 15140-122) in a humidified incubator with 5% CO2 at 37 ºC. HEK293H cells were seeded in 35 mm petri dish at a density of 2x10^5 cells per dish. HEK293H cells were rinsed two times with extracellular solution before experiments.

Cell culture and differentiation of hiPSCs. Following the previously reported protocol,[58] HiPSCs from reprogrammed fibroblasts (GM23338, Coriell Institute for Medical Research, NJ, USA) were cultured on Matrigel-coated plates (BD Biosciences) with stem basal medium (mTeSR1, STEMCELL Technologies) until reached 80-90% of confluence. Cardiac differentiation of iPSCs was initiated by treatment with 12 µM CHIR99021 (Tocris, 4423) diluted in RPMI/B27-insulin during the initial 24h; the medium was changed every day in succession for 3 days. Subsequently, hiPSCs were treated with 5 µM IWP4 (Tocris, 5214) that was diluted by RPMI/B27-insulin, which was removed after 24h. From day 4, hiPSCs were maintained in RPMI/B27-insulin with daily medium change. Spontaneous contractions of cardiomyocytes (CMs) were observed around 8-10 days after the initiation of the differentiation process. According to the previous protocol description,[59] CMs were purified by 5 mM L-lactate (Sigma, 71718) diluted in RPMI-glucose (Gibco, 11879-020), which was replaced daily in succession for 4 days. After purification CMs were dissociated with TrypLE Express (Gibco, 12605010) at 37 ºC for 15 min. Thereafter, the cell suspension was centrifuged for 5 min at 1500 RPM to remove the enzyme. Pellet of cells was mixed with RPMI/B27 insulin supplemented with fetal bovine serum 10% (Gibco, 16140-071), 1% Pen Strep (Gibco, 15140-122), and 5µM Y-27632 (Tocris 1254). For nanopipette injection, CMs were replanted in 35mm Matrigel coated dish at a density of 6x10^5 cells per dish. The spontaneous beating was observed around 5-6 days after replanting.

Nuclear staining of HEK cells. The staining of the live HEK nucleus is performed using the medium exchange method. Briefly, the original cell culture medium was removed and immediately replaced with a medium containing Hoechst33258 dye with ~1 µg/mL concentration. The cells were incubated at 37°C for 2 hours. Then the cells were washed with an extracellular medium twice before experiments.

Trypan blue (TB) exclusion test. The TB test was performed to evaluate the cell membrane damage due to nanopipette injection into the cell membrane.[60] Trypan blue was added to the extracellular medium in a 1:1 ratio to check the membrane integrity. After 10-15 min of incubation, optical bright field (BF) images were taken. The cells with intact cell membrane appear transparent as trypan blue cannot enter the cytosol. While cells with blue color represent the cell membrane damage and hence is a dead cell.

Fluorescence imaging. All fluorescence images were taken using a home-built inverted fluorescence microscope. A LED light source (X-cite 120 LED Boost, USA) was used to illuminate the sample. The emitted fluorescence light was collected by a 20x objective lens (Nikon, CFI S Plan Fluor ELWD) and recorded by a sCMOS camera (ThorLabs, USA).

Dark-field microscopy imaging. The dark-field (DF) microscopy images were taken by an inverted optical microscope (Nikon Eclipse Ti−U) equipped with a dark-field condenser (Nikon, Ti-DF, NA ∼0.8−0.95) and a 40× objective lens (Nikon CFI Super Plan Fluor ELWD, NA = 0.6). A CCD camera (Point Gray Grasshopper 3) was used to capture the dark-field images.

Data analysis and simulation. The electrical current and potential data were analyzed by using clampfit programs and Originpro 2018b. Moving average smoothing method with a 2 ms time window is typically applied to the data before statistical analysis. The dV/dt curves were smoothed by the moving average method using a 5 ms time window. ImageJ was used to analyze the fluorescence images. We used finite element method (FEM) simulation to solve coupled Poisson−Nernst−Planck (PNP) partial differential equations. To simplify the simulation, the fluidic flow term was not included, and the system was simulated at a steady state. COMSOL Multiphysics 5.2 with AC/DC and Chemical Reaction Engineering modules were used for the FEM simulation.

Results and Discussions

Optimizing Delivery and Single-Entity Detection in a Controlled Environment

Before the live-cell experiments, we first conducted the delivery and single-entity detection experiments by using the nanopore−CNE multifunctional nanopipettes in bath solution to optimize the experimental conditions and better understand the detection mechanism. The schematic of the experimental setup is illustrated in Figure 1a. To minimize the cellular damage induced by post intracellular delivery,[61] we used relatively long tapered (LT) nanopipettes with a shank length of about 6.2 ± 0.4 mm, as shown in Figure 1b. Based on the SEM image, the half cone angle of the nanopipette tip is ~3.5°. To better match the size of nanoentities, the nanopore diameter is in the range of 10-30 nm for biomolecules and 40-90 nm for GNPs. The average effective surface area of CNEs is estimated to be 0.24 µm^2. The exiting NPs have to pass through a long nanochannel before reaching the orifice of an LT nanopipette. The nanopipette tip geometry has been previously shown to affect greatly on resistive pulse signals.[37] Here, we mainly focused on the OCP detection by the CNE.

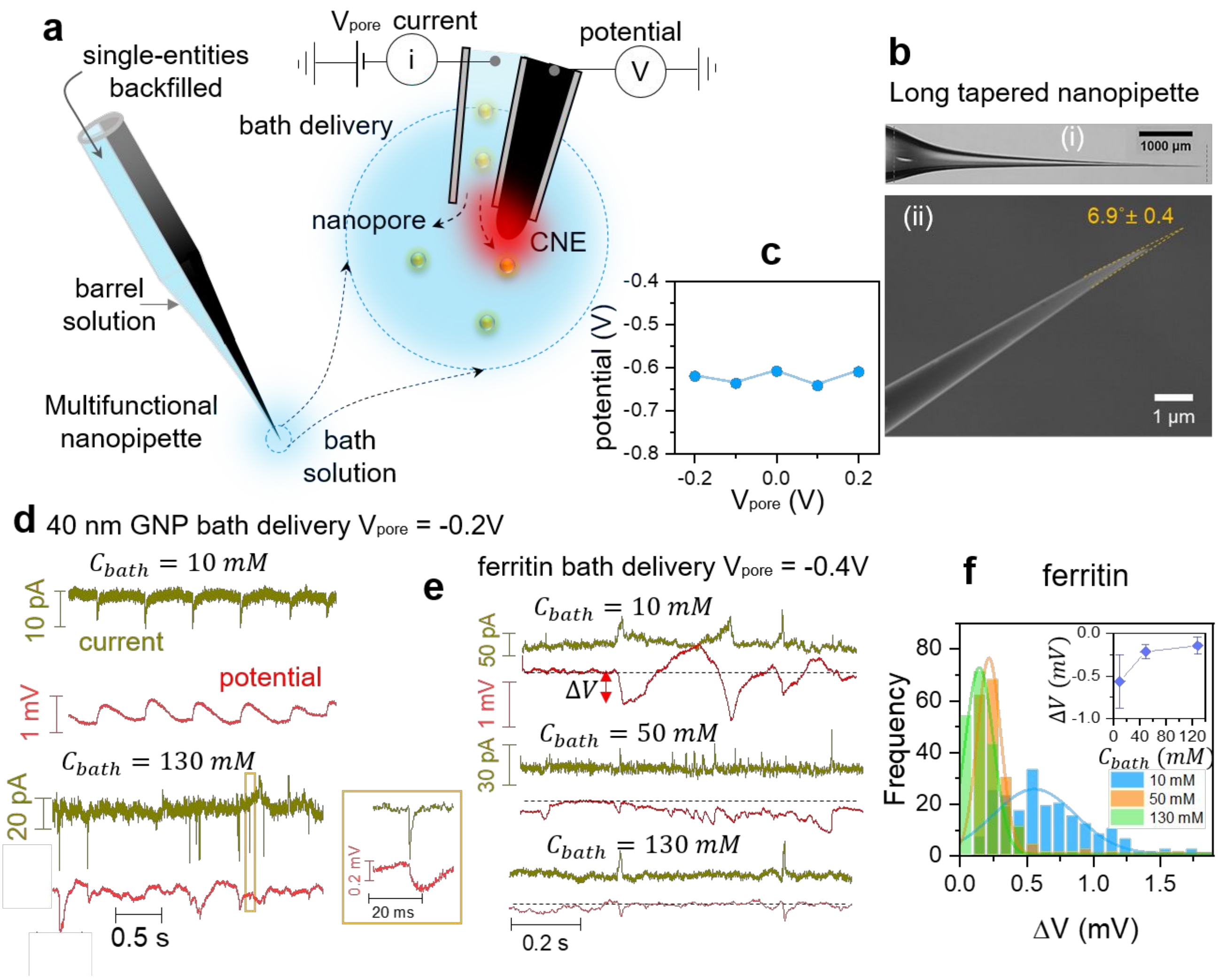

Figure 1: (a) The schematic experimental setup of the bath delivery and single-entity detection via a multifunctional long tapered nanopipette at V_{pore}=-0.2 V and with 130 mM PBS bath. The zoomed image of the nanopipette apex is also shown (not to scale). The V and V_{pore} are the potential on the floating CNE and the applied nanopore bias, respectively. The sensing zone of the CNE is shown as red color gradient. (b) Optical microscope (i) and SEM images (ii) of the side view of a LT nanopipette tip. (c) The baseline V *vs.* V_{pore} plot for a LT nanopipette at 130 mM PBS bath. (d) The *i-t* (olive) and *V-t* (red) time traces during the delivery of PEGylated 40 nm GNPs in (i) 10 mM (ii) 130 mM PBS bath. Zoomed-in current and potential changes in 130 mM PBS bath is also shown. (e) The *I-t* (olive) and *V-t* (red) time traces during bath delivery of ferritin with bath solution concentration of 10, 50 and 130 mM via a nanopipette at -0.4V V_{pore}. The black dashed lines denote potential baselines. (f) The histograms showing the ΔV distributions at different bath salt concentrations. N=208, 148, 200 for 10 mM, 50 mM and 130 mM PBS bath respectively. Solid lines in the histogram are Gaussian fits. The inset shows the plot of mean ΔV as a function of bath salt concentration. The error bars represent the standard deviation from mean.

The nanopore barrel is backfilled with 130 mM PBS solution (see the composition in method). Before adding proteins and/or NPs inside, both the *i*–*t* and *V*–*t* traces acquired respectively through the nanopore and CNE were stable and featureless at different nanopore bias V_{pore}. Figure 1c shows the potential baseline remains the same value at different V_{pore}. Therefore, the long channel of the LT nanopipette can effectively screen the changes of V_{pore} on the potential changes near the nanopore. After introducing nanoentities into the nanopore barrel, transient i and V changes often appeared in the time traces at the appropriate V_{pore}. These characteristic currents and potential changes are caused by the individual exiting entities via the orifice of the nanopore barrel. The nanoentities can be driven out by the applied V_{pore} through the electrokinetic effect. We typically applied the V_{pore} with a magnitude of 0.2 V from the beginning and optimized the V_{pore} in experiments based on the observed event rate. The polarity of V_{pore} normally depends on the charge polarity of the nanoentities.

Figures 1d shows the typical *i-t* and *V-t* traces at -0.2 V V_{pore} during the delivery of 40 nm PEGylated GNPs to 10 mM (i) and 130 mM (ii) PBS bath. The salt concentration is an important factor that influences the sensitivity of current and potential detections. In the 10 mM PBS bath, distinct and evenly spaced current spikes are observed. The uniformly distributed transient signals indicate the buildup of GNPs inside the nanopore barrel near the orifice.[62] Due to the strong electrostatic repulsion between the negatively charged GNPs and silica surface near the nanopore mouth, the motion of the exiting GNPs is slowed down, which is beneficial for the single-entity detection. In general, ~75% (7 of 9 attempts) of the GNP delivery in 10 mM PBS bath show highly correlated current and potential changes. However, delivery in 130 mM PBS bath features stochastic current spikes with shorter time duration t_D and bigger magnitude compared with the results in 10 mM PBS bath. Meanwhile, the potential changes fluctuate a lot in shape and magnitude. Less than 20% (2 of 6 attempts) of the experiments show highly correlated potential changes. The mean magnitude of the transient potential changes (ΔV) is generally smaller. These differences are attributed to the faster GNP movement and reduced potential sensitivity when the bath solution salt concentration is high.

We also studied the single-entity detection of biomolecules by delivering ferritin proteins (d=11 nm, pI=5.4) into the bath solution. Figure 1e shows the typical current and potential time traces during the ferritin protein delivery at V_{pore}=-0.4 V with 10, 50, and 130 mM bath salt concentration. Similar to the GNP results, the transient potential change is bigger and the current and potential correspondence is better at low (10 mM) salt concentration. The mean ΔV as a function of bath concentration is shown in Figure 1f. The mean ΔV decreases with the increase of bath concentration.

To better understand the potential sensing mechanism for intracellular delivery, FEM simulations are performed at the steady state. Figure 2a shows the simulation model and the

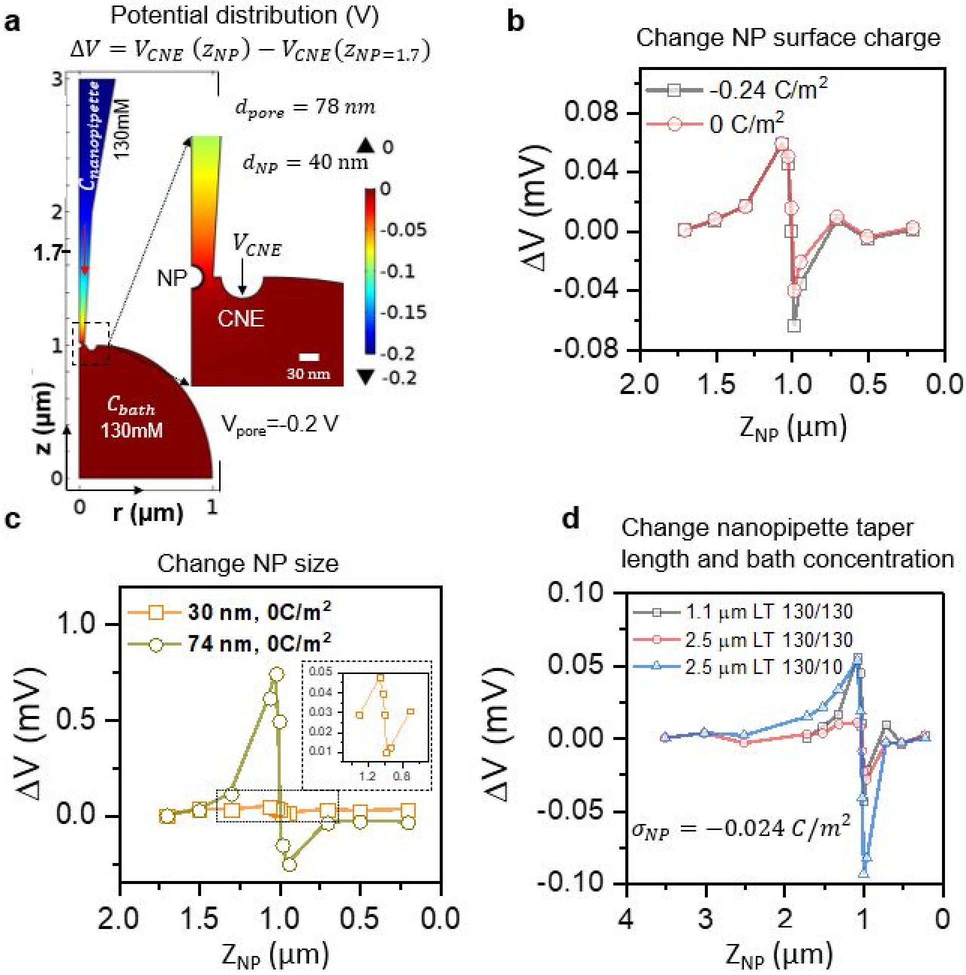

Figure 2: (a) The simulation model and the electric potential distribution when a NP is at the nanopore (r=0, z=1) in 130 mM KCl bath. The concentration inside the nanopipette is always 130 mM. A 3 nm thick insulating layer is placed on top of a 40 nm GNP to mimic the structure of PEGylated GNP. The GNP surface charge density is -0.024 C/m². The nanopipette surface charge density is -0.005 C/m². There is no charge on the floating CNE surface. The downward red arrow denotes the NP motion direction. The nanopipette tip region is zoomed in the right. Scale bar is 30 nm. (b) The simulated ΔV vs. z_{NP} plots for the 40 nm NP with -0.24 C/m² and 0 C/m² surface charge densities. (c) The ΔV vs. z_{NP} plots for neutral dielectric NPs with 30 nm and 74 nm sizes. The plot in the dashed rectangle is zoomed in the inset. (d) ΔV vs. z_{NP} plots for a 40 nm NP delivery from nanopipettes with 1.1 μm and 2.5 μm taper lengths and at different bath salt concentrations. 130/10 denote nanopore barrel / bath salt concentrations. We used the V_{CNE} (Z_{NP}=3.5 μm) as the reference point here.

potential distribution with 130 mM KCl solution in both bath and barrel when a NP is at the orifice. To compare with the experiment results, we monitor the change of CNE potential (V_{CNE}) when the NP is positioned at different z locations along the symmetry axis r=0. To quantify the change of V_{CNE} (ΔV) induced by the NP position change, we define a refence point (r=0, z=1.7 μm) far away from the CNE. Near and beyond this point, the presence of NP has no impact on the V_{CNE}.

We first investigate the effect of surface charge of NP on the ΔV change. As shown in Figure 2b, the ΔV magnitude is maximum when the NP is at the orifice and zero when the NP is far away (z=±1.7 μm). The shapes of ΔV-z_{NP} plots are always biphasic. When the NP is negatively charged (*i.e.* $-0.24 C/m^2$), the downward peak becomes slightly higher but remains the biphasic shape. This is different from the mainly downward peak shape for the negatively charged NPs at low salt concentration.[53, 62] Here, the biphasic shape is mainly due to the resistive changes induced by the NP translocation motion. The charge sensing mechanism-based potential detection become minor at the high salt concentration.

Because the ΔV during delivery is mainly due to the resistive change at the high salt concentration, the size difference between the NP and nanopore should impact ΔV. As shown in Figure 2c, when the NP is only 30 nm while the nanopore size is 78 nm, the ΔV vs z_{NP} plot has a biphasic shape but the change is very small (see the inset of Figure 2c). When the NP size is increased to 74 nm, the ΔV change is about 10 times bigger. Therefore, the size match between NP and nanopore plays a significant role for ΔV. Both the nanopore current sensing and CNE OCP sensing can achieve a higher sensitivity when the nanopore size is comparable to the NP size.

The taper length of the nanopipette can also impact the measured ΔV. As shown in Figure 2d, two nanopipette geometries were simulated with charged glass wall lengths of 1.1 μm and 2.5 μm. The ΔV change as a function of Z_{NP} induced by the NP through the 1.1 μm nanopipette in 130 mM KCl bath is biphasic (gray) while the ΔV change with the 2.5 μm nanopipette is more of a downward dip (red). We also simulated the ΔV change via the 2.5 μm nanopipette in a 10 mM KCl bath. A much larger biphasic ΔV change is observed (blue), demonstrating the effect of bath salt concentration.

The FEM simulation results suggest the potential sensing at high salt concentration is quite different from the case at low salt concentration. In general, the ΔV change is smaller and the resistance change induced potential redistribution is the main cause of the potential change at the CNE. Because of the same resistive change origin, the potential change and current change are expected to be highly correlated. Meanwhile, the ΔV can be affected by several other factors, including nanopipette tip geometry, NP surface charge and size match, and local salt concentration, which may lead to highly variable ΔV shape. It should also be noted that the simulation is at a steady state. The contribution of NP motion cannot be simulated. As shown in Figure 1d, at the low bath salt concentration, the GNP motion is much slower, which also helps to achieve a better SEE signal. Due to the molecular crowding effect inside the cell, we also expect the nanoentities will come out of the nanopore mouth slower.

Multifunctional Nanopipette for Intracellular Injection

The experimental setup for the voltage-controlled intracellular delivery of single-entities via a multifunctional nanopipette is illustrated in Figure 3a. The nanopore barrel is filled with an intracellular medium containing nanoentities. The nanopipette tip position is controlled by a micromanipulator and monitored using an optical microscope. The micromanipulator has three fine orthogonal control knobs each with a spatial resolution of 60 nm. The intracellular delivery of the nanoentities is accomplished by applying a proper V_{pore} to the nanopore barrel. Meanwhile, we record the current and potential changes, which helps to guide the delivery process. The delivery efficiency, as well as the distribution of the delivered biomolecules within a cell, is then characterized by fluorescence microscopy.

Figure 3b shows the typical current (olive) and potential (red) time traces during the (i) approach and insertion, (ii) delivery of FITC dye, and (iii) retraction of a multifunctional nanopipette tip. The corresponding optical images for each step are also shown on the top. In step (i), before the nanopipette tip reaches the cell membrane, the current baseline at V_{pore} = 0.1 V is stable and flat. Since FITC dye has a net negative charge of -1.02e,[63] the positive V_{pore} bias is applied to prevent the leakage of the dye in the bath. When the nanopipette tip makes contact and punctures the cell membrane, characteristic ionic current drop in steps are observed (see the zoom-in trace). In step (ii), with the tip inside the cell, the V_{pore} is changed to negative to begin the delivery of FITC dye molecules. Most of the delivery is finished in 2-4 minutes. When the delivery is finished, V_{pore} is switched back to 0.1V. Finally, in step (iii), the nanopipette tip is retracted from the cell and detached from the cell membrane. Similar to step (i), we can observe a step-wise increase of baseline current (see the zoom-in trace). It is worth noting that we can also observe the potential changes during the tip insertion and retraction. The potential changes normally happen earlier than the corresponding current changes, which is attributed to the longer potential detection range. However, the potential baseline is also noisier.

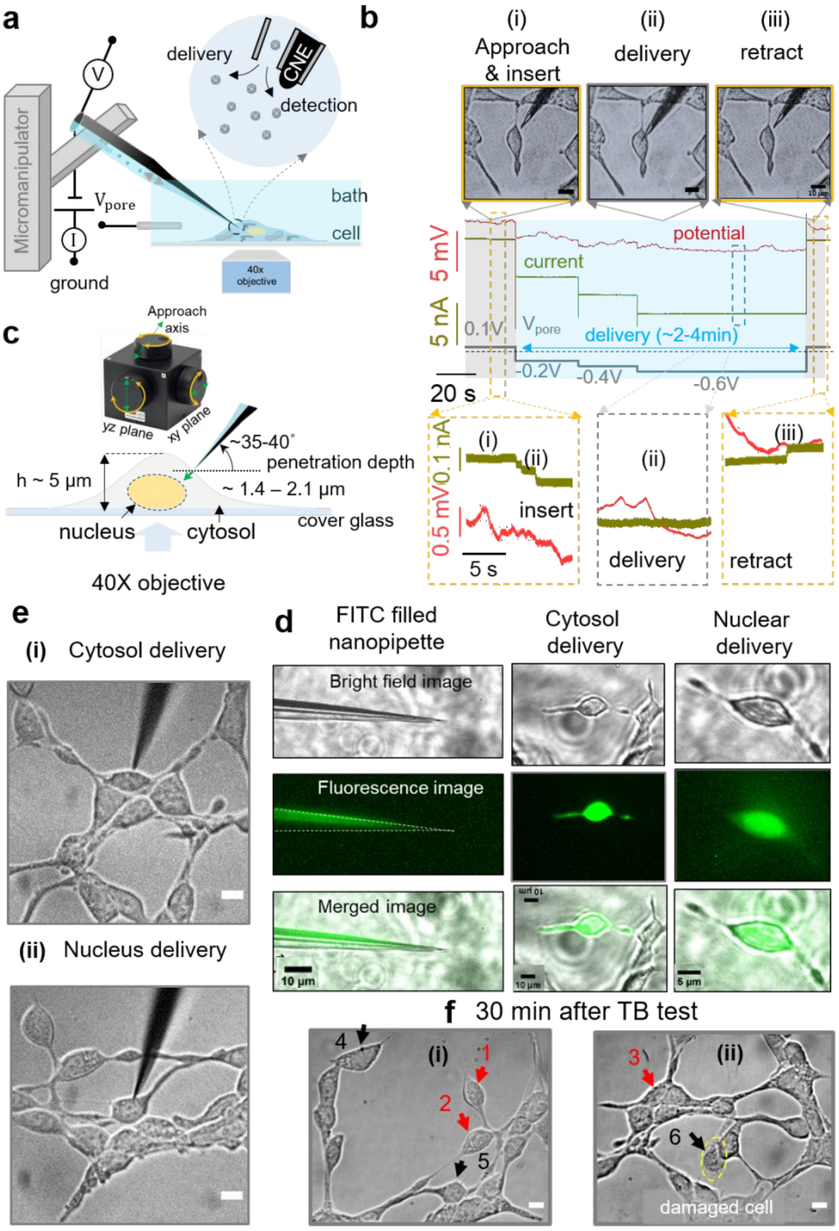

Figure 3: (a) The schematic experimental setup of the intracellular delivery of single-entities via a multifunctional nanopipette. The extracellular bath solution is grounded and V_{pore} is the bias applied to the nanopore barrel filled with intracellular medium. High impedance differential amplifier connected to CNE-barrel to measure the local potential change at the floating CNE. (b) Typical *i-t* (olive) and *V-t* (red) traces during approach and insert (i), 2-4 min delivery (ii) and retraction (iii) of a multifunctional nanopipette. (c) The schematic of a controlled cytosol vs. nucleus injection into cell via multifunctional nanopipette using a high precision micromanipulator. Top inset in (c) show the three fine orthogonal control knobs with 60 nm resolution. (d) Optical images of (i) cytosol and (ii) nucleus delivery on HEK cells. (e) The fluorescence images of FITC filled multifunctional nanopipette and cytosol and nucleus delivery of 20 µM of FITC dye. The merged fluorescence image shows the cytosol and nucleus delivery. (f) The optical images of cells 30 min after TB exclusion test to evaluate cell viability post-delivery. (i, ii) Cells labelled with 1, 2, 3 and 4, 5, 6 arrows denote cytosol and nucleus intracellular medium delivered cells respectively. The arrows denote injection point. Dotted encircled cell 6 was intentionally damaged. Scale bars 10 µm.

As illustrated in Figures 3c and 3d, the inserted nanopipette tip can be controlled by the fine approach axis control knob of the manipulator to stay in the cytosol or further insert into the nucleus of the HEK293 cell in step (ii). Figure 3e presents the fluorescence images of FITC filled nanopipette tip (i) and HEK cells after cytosol (ii) and nucleus (iii) deliveries. During the cytosol delivery, the nanopipette tip is inserted ~1 µm deep inside the cell. The fluorescent dye molecules can diffuse quickly to evenly distribute the entire cytosol and even diffuse to the neighboring cells through intercellular connections. If the nanopipette tip penetrates more than 2 µm, the tip can often get into the nucleus to enable nucleus delivery. The fluorescent image in Figure 3e(iii) reveals that the majority of the dye molecules are concentrated around the nucleus.

To evaluate the cell membrane damage due to the delivery of nanoentities via nanopipette, a TB exclusion test was performed after the delivery process. The delivery experiments were conducted at the typical conditions for 3-5 min. The cytosol delivery cells (labeled 1 through 3 in Figure 3f) and the nucleus delivery cells (labeled 4 and 5 in Figure 3f) did not change color after treating the cells with TB for more than 30 min, confirming the integrity of the cell membrane. In contrast, when the membrane was intentionally damaged by inserting the nanopipette tip much deeper (i.e. >3 µm) into the cell (cell 6 in Figure 3f (ii)), the cell only appeared slightly darker in the grayscale BF image taken by the monochromatic CCD camera (slightly blue by eye).

The delivery efficiency of this method is high. Typically, one nanopipette can conduct up to 5-8 intracellular deliveries within 20-30 min with a delivery efficiency of 80-90%.

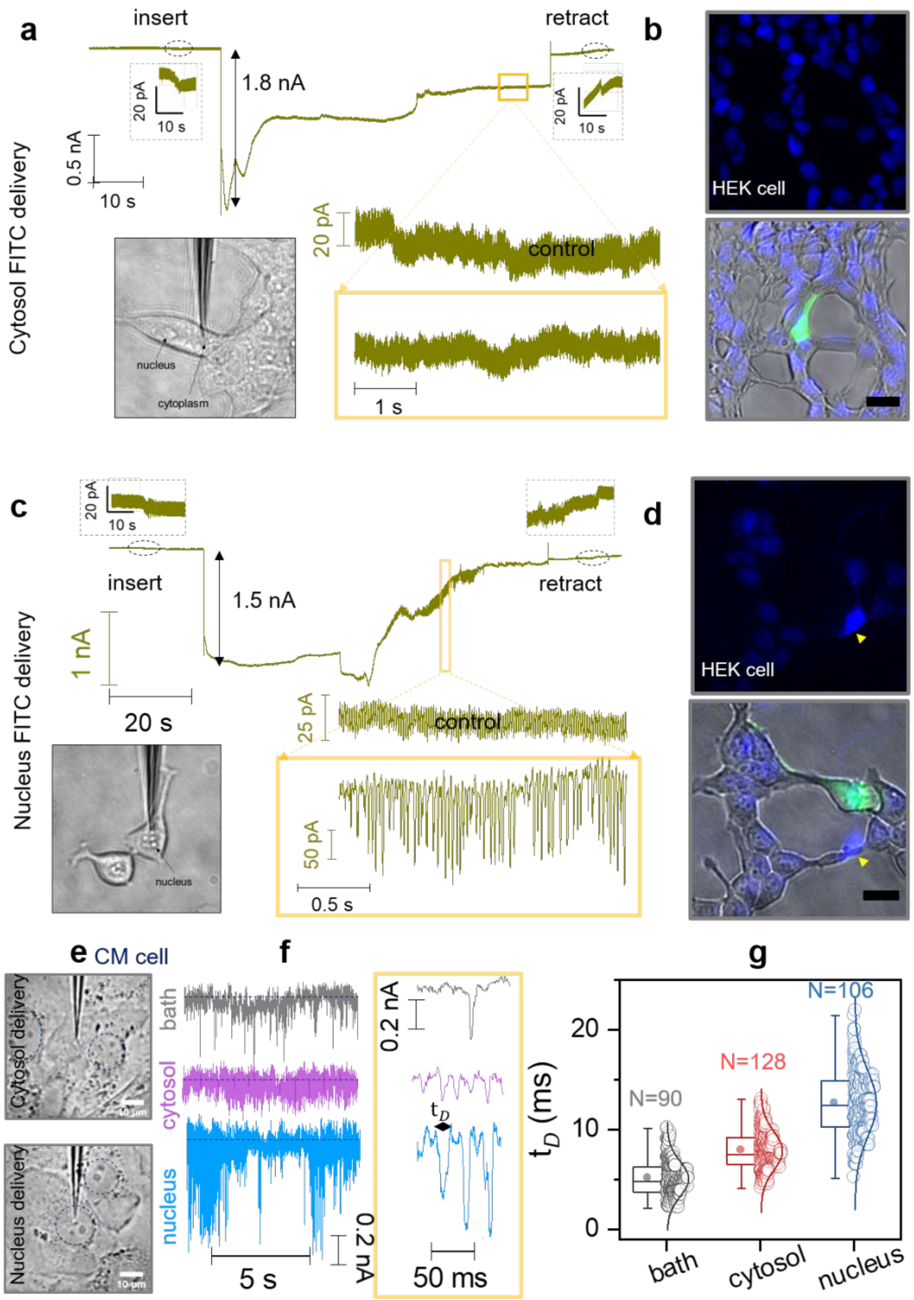

Figure 4: (a-b) The *i-t* trace (a) of cytosol delivery of fluorescent FITC molecules in HEK cells at V_{pore}=-0.5 V and the corresponding fluorescence and the merged (fluorescence and bright-field) images (b). Hoechst33258 dye (violet) was used to stain the nucleus and green fluorescence is from FITC dye. Scale bars 10 µm. (c-d) The *i-t* trace (c) of nucleus delivery of fluorescent FITC molecules in HEK cells and the corresponding fluorescence and merged images (d). The bright blue fluorescence in d is due to a floating dead cell. The current change due to the insertion and retraction of the nanopipette tip is shown in zoomed image. The highlighted sections in (a) and (c) are zoomed below. Single barrel quartz nanopipette with pore diameter of ~ 10 nm was used in the experiment. (e) The bright field images of CM cytosol and nucleus ferritin delivery. The dashed circle denote the nucleus of the CM cells. (f) Current time traces of bath (gray), cytosol (purple) and nucleus (blue) delivery of ferritin in CM cells and respective zoomed traces are shown in the right. (g) The bar chart for the t_D results in bath delivery, and CM cell cytosol and nucleus deliveries of ferritin.

The Ionic Current Based Single-Molecule Detection of Delivered Molecules in Live Cells

Though the delivery of small fluorescent dye molecules into HEK cells is successful, transient current and potential changes induced by the exiting of individual dye molecules cannot be observed due to the relatively large average pore diameter (20 nm). Owing to the poor sensitivity of potential detection on the very small dye molecules, we used single barrel quartz nanopipettes with small pore diameter (<15 nm) to investigate the intracellular single-molecule detection of the delivered molecules by nanopore current.

We first inserted the nanopipette tip in the cytosol of HEK cells, as shown in the optical microscope image in Figure 4a. The typical i-t trace during the cytosol delivery of FITC dye molecules is also shown. No clear current spikes can be resolved. This is common in ~70% of the cytosol deliveries of FITC we conducted. Therefore, the nanopore current sensitivity is still poor for the delivered FITC molecules in the cytosol. To confirm the delivery is successful, we took fluorescence images after the dye delivery. As shown in Figure 4b, the green fluorescence intensity of FITC is uniform inside the delivered cell, confirming the successful cytosol delivery of the dye molecules.

We then inserted the nanopipette tip in the nucleus, as shown in the optical image in Figure 4c. A typical i-t trace during nucleus delivery of FITC dye molecules is shown in Figure 4c. Interestingly, the *i-t* trace features numerous distinguishable current spikes, corresponding to individual delivered dye molecules. The increase in the nanopore sensitivity to enable single dye molecule detection can be attributed to the increased molecular crowding effect inside the nucleus. The fluorescence intensity image post-nucleus delivery is presented in Figure 4d. The green fluorescence intensity is obviously non-uniform inside the cell and is higher at the nucleus, confirming the nucleus delivery.

We further compared the *i-t* traces of cytosol and nucleus delivery in Figures 4a and c. When the intracellular delivery began by switching the V_{pore} to -0.5 V, the overall current change magnitude in cytosol delivery (1.8nA) is ~17% larger than that in the nucleus delivery (1.5 nA). This is attributed to the bigger access resistance when the tip is in the nucleus. During the delivery, the magnitude of the current baseline keeps decreasing towards zero. The current drop is more obvious in the nucleus delivery. The drop in the current baseline indicates the accumulation of the dye molecules near the orifice, which is attributed to the slowed dissipation of dye molecules. The dense environment of the nucleus further retarded the motion of dye molecules, leading to the clogging effect. As we discussed in section 1, the slowed movement of the molecule is actually beneficial for nanopore detection. Indeed, the single-molecule current spikes in the nucleus delivery often appeared after the partial reduction of the current baseline.

To verify the effect of the intracellular environment on the nanopore detection, we also conducted the delivery experiments of negatively charged ferritin proteins (about 11 nm in size) to the hiPSC derived CM cells and compared the current signals between cytosol and nucleus deliveries. Figure 4e shows the optical BF images during the delivery of ferritin into cytosol and nucleus of a CM cell. The nucleus of the CM cell circled by the dashed line can be resolved in the images. Figure 4f shows the corresponding i-t traces during the delivery. Compared with the i-t trace of the control experiment with no ferritin molecules, high-density current spikes are observed in

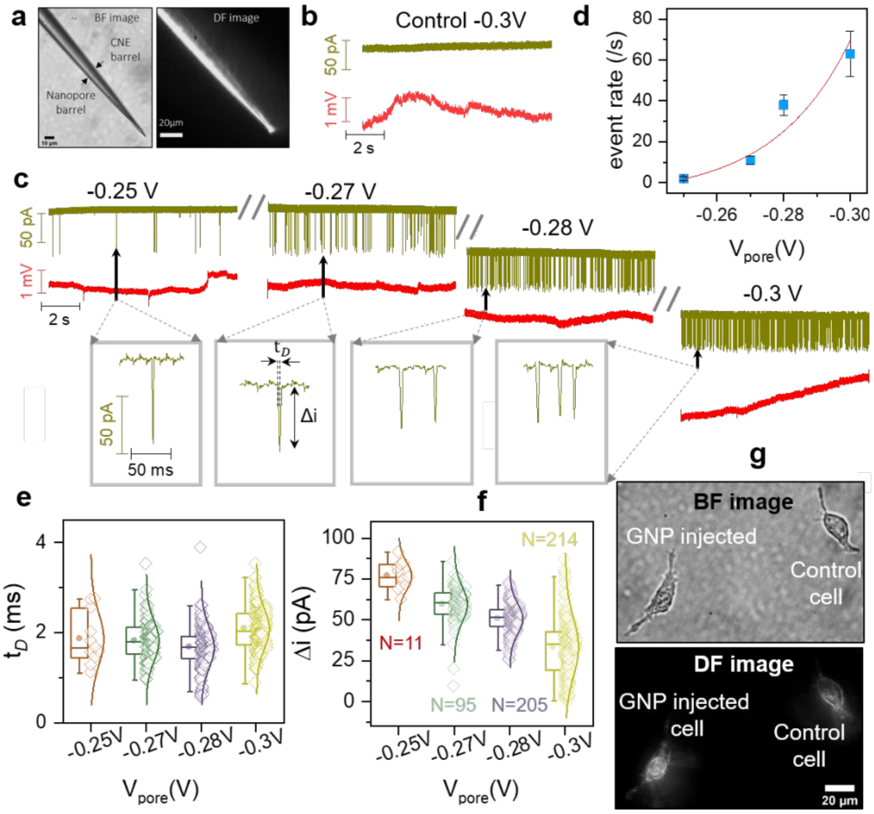

Figure 5: (a) BF and DF images of 40 nm PEGylated GNP filled multifunctional nanopipette. (b) *I-t* (olive) and *V-t* (red) traces during intracellular medium (b) and GNP (c) delivery into HEK cell via a nanopipette. Zoomed current spikes at all V_{pore} are also shown inside gray rectangle. (d) The V_{pore} effect on the event rate (/s) of intracellular GNP delivery. The error bars represent the standard deviation from three measurements each of 10 s duration. Solid red line is the exponential fit. The bar chart of current t_D at different V_{pore}. (e) The bar plot of current spike t_D at different V_{pore}. (f) The bar plot of current spike amplitude (Δi) at different V_{pore}. (g) The BF and DF images after delivery of GNP into HEK cell. The DF image of the HEK cell without GNP delivery is also shown as control.

both cytosol and nucleus deliveries. Between the traces during cytosol and nucleus deliveries, the current spikes are generally more distinguishable for the nucleus delivery. The statistical analysis of the current spike duration time (t_D) for bath, cytosol and nucleus deliveries is shown in Figure 4g. The mean t_D for bath, cytosol and nucleus deliveries are 4.7 ± 1.6 ms, 7.5 ± 1.9 ms and 12.5 ± 3.7 ms, respectively. The mean t_D is least for bath delivery and highest for the nucleus delivery. The mean t_D for cytosol and nucleus deliveries is ~1.6 and 2.6 times higher than that of bath delivery. Therefore, the exited ferritin is slowed down by the crowded environment of the cytosol and nucleus, which enhancing the nanopore sensitivity. The cellular environment thus plays an important role in SEE detection. The single-entity signal may also be used to probe the cellular environment of different organelles in a cell or different cells.

The Intracellular Delivery and Single-Entity Detection of GNPs in HEK Cells

To test the intracellular delivery and detection of large NPs, 40 nm PEG-GNPs are also delivered into the HEK cells using multifunctional nanopipettes tips. The nanopipettes for GNP delivery have a mean nanopore diameter of 64 ± 7 nm. Figure 5a shows the BF and DF images of a PEG-GNP filled multifunctional nanopipette tip. The CNE barrel is dark and the nanopore barrel is bright in the BF image. While, in the DF image, the nanopore barrel is much brighter due to the enhanced scattering light from the loaded GNPs.

Figure 5b shows the *i-t* (olive) and *V-t* (red) traces during the intracellular medium delivery into the HEK cytosol at V_{pore}=-0.3V. The *i-t* trace is featureless during intracellular medium delivery. Figure 5c shows the typical *i-t* (olive) and *V-t* (red) traces during the delivery of PEG-GNPs into the HEK cytosol at different negative V_{pore} biases. Compared with the small dye molecules and ferritin, the intracellular current detection of larger size GNP is relatively easy. Many current spikes appeared in the *i-t* trace, confirming the successful intracellular delivery of GNPs. Compared with the current spikes in the 130 mM bath solution (Figure 1c), the current spikes here are denser with bigger magnitudes though a slightly higher negative V_{pore} is needed to drive the GNPs out. This is attributed to the more crowded cytosol. Representative individual current spikes at different V_{pore} are also shown in the insets. Different from the current signal, the V-t trace shows rare corresponding transient changes during the GNP delivery. Therefore, intracellular potential sensing is still challenging in the cytosol of HEK cells.

Based on the current spikes, the plot of event rate (/s) as a function of V_{pore} is shown in Figure 5d. The GNP delivery rate increased exponentially with the V_{pore}. At -0.25 V, the event rate for the GNP delivery is about 0.7/s. While at -0.3 V, the event rate reaches ~61/s. Statistical analysis of t_D and Δi are shown in Figures 5e and f. Interestingly, with the increase of the V_{pore} magnitude, the mean amplitude of Δi is obviously reduced and the mean t_D is slightly increased. This is opposite to the general results of nanopore translocation events. We attribute these results to the increased GNP accumulation at the vicinity of the delivery region due to the quickly increased delivery rate at the higher magnitude of V_{pore}. Due to the crowded intracellular environment, the delivered GNPs in the cytosol cannot dissipate away quickly. They generated the extra resistance for the newly delivered GNPs and slowed down their movement, leading to increased t_D and decreased Δi. Because the current baseline did not change obviously, the accumulation of GNPs should be slightly away from the nanopore orifice, which did not result in the clogging of the nanopore.

To confirm the successful delivery of GNPs into the cytosol of HEK cells, DF imaging was performed. Figure 5g shows both the BF and DF images of the cells after ~3 min of GNP delivery. Compared with the control cell, the cytosol of the GNP-delivered cell appeared brighter post-injection due to the strong scattering of the GNPs.

The Delivery and Detection of GNPs in Individual HiPSC Derived CMs

So far, we have achieved intracellular single-entity detection by ionic current but not the potential. The FEM simulations revealed that the potential detection is impacted by several factors. We have found that it is sensitive to the changes in the local cell environment such as ion concentration and crowding. To understand the effect of different cell environments on the potential detection sensitivity, PEG-GNPs is also delivered into the hiPSC-CMs using multifunctional nanopipettes. The nanopipettes used in intracellular delivery of HEK and CMs cells have the similar nanopore diameter.

Figure 6a shows the *i-t* (olive) and *V-t* (red) traces of PEG-GNP delivery into the cytosol of hiPSC-CMs under different V_{pore}. The current and potential spikes are very clear with high signal-to-noise ratios. Similar to the case of HEK delivery, the delivery rate is very sensitive to the magnitude of the applied V_{pore}. As shown in Figure 6b, the delivery rate of GNP at -0.3 V is ~ 0.8/s. While at -0.9 V, the delivery rate reaches ~24/s. Compared with the case of HEK delivery, the delivery rate is about 2.5 times lower while the V_{pore} magnitude is 3 times higher, reflecting the bigger delivery resistance in the CM cytosol.

Statistical analysis of Δi and ΔV are shown in Figures 6c and d. Compared with the results of HEK in Figure 5, the magnitude of mean Δi is much higher and the ΔV can be detected. In addition, the Δi and ΔV are gradually increased while t_D (not shown) gradually decreased on increasing V_{pore}. The gradual increase of Δi and ΔV and decrease of t_D suggest the typical electrophoretic driven delivery of PEGylated GNPs. Therefore, unlike the delivery of GNPs into HEK, the effect of GNP accumulation near the tip is not obvious. The different results in different cells can be attributed to the lower delivery rate in CMs, which allows more time for the delivered GNPs to dissipate away from the tip. The GNPs may also dissipate better once inside the CMs under the higher V_{pore}.

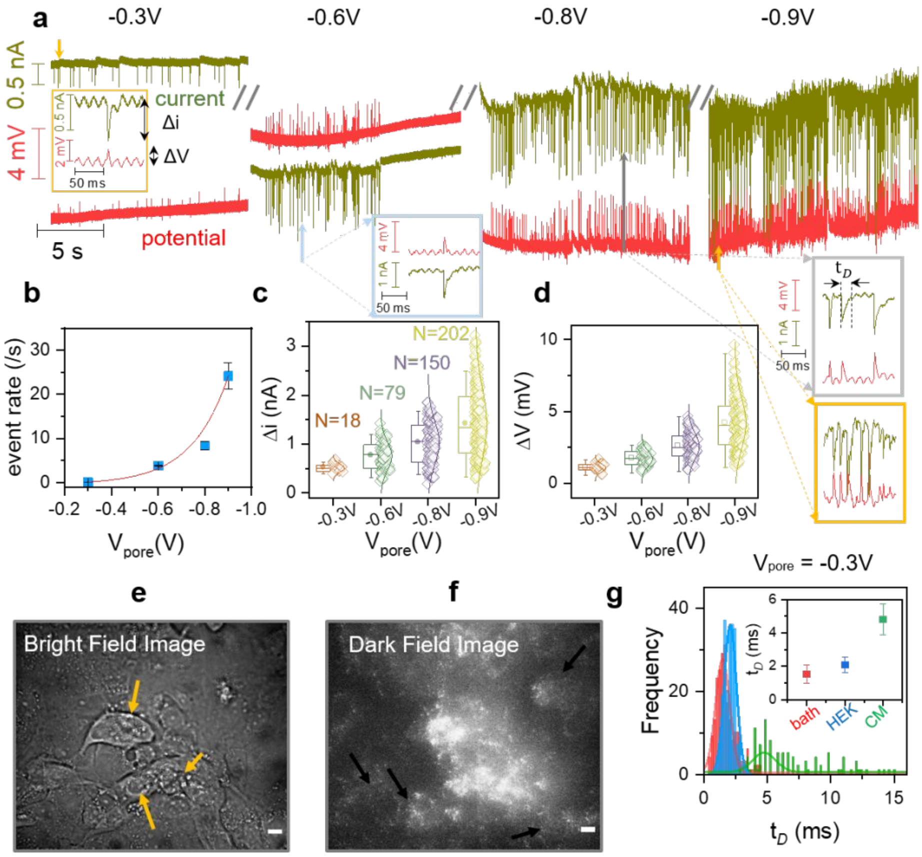

Figure 6: Controlled intracellular delivery of PEGylated GNP into CM cells using a multifunctional nanopipette. (a) Representative *i-t* (olive) and *V-t* (red) traces of PEGylated GNP delivery into CMs at various V_{pore}. The zoomed current spikes corresponding to each V_{pore} is shown below. (b) The delivery rate (/s) as a function of V_{pore}. Solid red line is the exponential fit. The 15 s of PEG-GNP delivery data was considered to estimate event rate. The error bars represent the standard deviation from three measurements each of 15 s duration. (c-d) The bar plots of Δi vs. V_{pore} (c) and ΔV vs. V_{pore} (d). (e) BF and (f) DF images of PEGylated GNP delivered CM cells. The yellow arrows in (e) denote the nanopipette insertion locations and black arrows in (f) show the DF image of CMs with no PEG-GNP delivery. Scale bars 20 µm.(g) Histograms showing the t_D comparison during bath and PEGylated GNP delivery into HEK (Figure 5c) and CM cells at V_{pore} = -0.3V. N= 221, 214 and 112 for bath, HEK and CM delivery respectively. The inset show the corresponding t_D plot. Error bar denote the standard deviation from the mean. The solid lines on the histogram denote the Gaussian fits.

To confirm the successful delivery of PEG-GNPs into the cytosol of CMs, DF imaging was performed. Figures 6e and f, respectively, show the BF and DF images took about 20 min after the delivery. Compared to the control cells where no PEG-GNPs were injected (cells indicated by the black arrows in Figure 6d), the cytosol of the PEG-GNP delivered CM cells (cells indicated by the yellow arrows in Figure 6c) appeared brighter due to the scattering of the GNPs.

The major difference between the results in HEK and CM cells is the appearance of highly correlated current and potential signals in the time traces. The individual current and potential peaks can be clearly seen in the insets of Figure 6a. The potential peaks are always upward, suggesting the sensing mechanism is not based on charge. Based on the FEM simulation results in Figure 2, the highly correlated upward potential peaks can be attributed to the big local resistance changes induced during the GNP translocation. We also conducted the t_D analysis of current spikes. Figure 6g shows the histograms of the t_D at the same V_{pore} (-0.3 V) for both bath and intracellular delivery of PEG-GNPs. The mean t_D is the least for bath delivery and the highest for CM delivery. About four-fold increase of t_D was observed between bath and CM cytosol deliveries. About three-fold increase of t_D was observed between HEK and CM cytosol deliveries. The significant increase of t_D in CM delivery suggests that the motion of the GNPs is further slowed down during the CM delivery, which can explain the higher SEE sensitivity in the CMs. The observed larger t_D in CMs may be induced by the more complex cellular structure of CMs, such as sarcomere, t-tubules and SERCA, which are absent in the HEK cells.

Conclusions

In summary, we have demonstrated the feasibility of using nanopore-CNE multifunctional nanopipette for voltage-controlled, minimally-invasive, targeted intracellular delivery with *in-situ* single-entity detection capability. Through control experiments in bath solution and FEM simulations, we showed the nanopipette with the long taper geometry was suitable to conduct intracellular delivery and single-entity detection simultaneously. We also investigated the sensing mechanism of OCP detection by CNE in near physiological salt concentration. Instead of charge sensing, the CNE mainly detects the local potential change induced by the drastic resistance change during the translocation of nanoentities. We have showed that various nanoentities, including dye molecule, ferritin protein and 40 nm GNPs, can be delivered into the HEK and CM cells in a controlled fashion with high efficiency. Meanwhile, the SEE detection of these nanoentities during delivery are achieved.

Interestingly, the current and potential SEE signals are strongly affected by the local environment near the nanopipette tip. Compared with the results in the bath solution, the current single-entity signals of nanopore show improved signal-to-noise ratio. For example, we can detect individual small dye molecules delivered in cytosol of HEK cells by the nanopore but not in the bath solution with the similar salt concentration. By using micromanipulator, we selectively deliver the nanoentities to cytosol or nucleus of cells. The SEE sensitivity is always higher during the nucleus delivery. For the cytosol delivery results between HEK and CM cells, we always observed the higher SEE sensitivity in CMs. The single-entity potential sensing by CNE can be achieved in the CMs but not in the HEK cells. These results are attributed to the molecular crowding effect. As suggested by the duration time of current spikes, the movement of the nanoentities via a nanopore is slower with the increase of the crowding effect. The slower movement of the exiting nanoentities can effectively enhance the SEE detection.

With the assistance of the SEE signals, we can improve the accuracy of the delivery and monitor the delivery process and the cellular response in greater details, which cannot be achieved by the fluorescence imaging. For example, when the entities are delivered very fast, we can detect the accumulation of delivered entities near the nanopipette tip. With the instant feedback by SEE signals, we can control the delivery rate, thus reducing the aggregation induced cellular damage and nanopieptte clogging. We believe this developed platform is ideal for single-cell studies with both cellular manipulation and detection functions.

Conflicts of interest

There are no conflicts to declare.

Acknowledgements

This work was partially supported by National Science Foundation (NSF) Grants CBET-1454544 and the NSF Engineering Research Centers Program under NSF Cooperative Agreement EEC-1647837. The authors want to thank Prof. Fenfei Leng for the help of nucleus staining method and Govinda Ghimire for preparing PEGylated GNPs. P.P also acknowledges the support of the FIU CASE distinguished postdoc fellowship.

References

1. W. Poon, B. R. Kingston, B. Ouyang, W. Ngo and W. C. W. Chan, *Nature Nanotechnology*, 2020, **15**, 819-829.
2. D. Kim, C.-H. Kim, J.-I. Moon, Y.-G. Chung, M.-Y. Chang, B.-S. Han, S. Ko, E. Yang, K. Y. Cha, R. Lanza and K.-S. Kim, *Cell Stem Cell*, 2009, **4**, 472-476.
3. M. P. Stewart, A. Sharei, X. Ding, G. Sahay, R. Langer and K. F. Jensen, *Nature*, 2016, **538**, 183-192.
4. M. P. Stewart, R. Langer and K. F. Jensen, *Chemical Reviews*, 2018, **118**, 7409-7531.
5. N. P. Restifo, M. E. Dudley and S. A. Rosenberg, *Nature Reviews Immunology*, 2012, **12**, 269-281.
6. R. Duangrat, A. Udomprasert and T. Kangsamaksin, *Cancer science*, 2020, **111**, 3164-3173.
7. A. D. Fesnak, C. H. June and B. L. Levine, *Nature Reviews Cancer*, 2016, **16**, 566-581.
8. L. Warren, P. D. Manos, T. Ahfeldt, Y.-H. Loh, H. Li, F. Lau, W. Ebina, P. K. Mandal, Z. D. Smith, A. Meissner, G. Q. Daley, A. S. Brack, J. J. Collins, C. Cowan, T. M. Schlaeger and D. J. Rossi, *Cell Stem Cell*, 2010, **7**, 618-630.
9. L. Rohani, C. Fabian, H. Holland, Y. Naaldijk, R. Dressel, H. Löffler-Wirth, H. Binder, A. Arnold and A. Stolzing, *Stem Cell Research*, 2016, **16**, 662-672.
10. C. J. Bishop, J. Kim and J. J. Green, *Annals of biomedical engineering*, 2014, **42**, 1557-1572.
11. S. Patel, A. Athirasala, P. P. Menezes, N. Ashwanikumar, T. Zou, G. Sahay and L. E. Bertassoni, *Tissue Engineering Part A*, 2018, **25**, 91-112.
12. U. Rothbauer, K. Zolghadr, S. Tillib, D. Nowak, L. Schermelleh, A. Gahl, N. Backmann, K. Conrath, S. Muyldermans, M. C. Cardoso and H. Leonhardt, *Nature Methods*, 2006, **3**, 887-889.
13. A. K. Fajrial, Q. Q. He, N. I. Wirusanti, J. E. Slansky and X. Ding, *Theranostics*, 2020, **10**, 5532-5549.
14. T. K. Kim and J. H. Eberwine, *Analytical and bioanalytical chemistry*, 2010, **397**, 3173-3178.
15. E. Neumann, M. Schaefer-Ridder, Y. Wang and P. H. Hofschneider, *The EMBO Journal*, 1982, **1**, 841-845.
16. P. Actis, *Small Methods*, 2018, **2**, 1700300.
17. F. Tang, K. Lao and M. A. Surani, *Nature Methods*, 2011, **8**, S6-S11.
18. S. S. Rubakhin, E. V. Romanova, P. Nemes and J. V. Sweedler, *Nature Methods*, 2011, **8**, S20-S29.
19. J. R. Heath, A. Ribas and P. S. Mischel, *Nature Reviews Drug Discovery*, 2016, **15**, 204-216.
20. Y. Zhang, C. B. Ballas and M. P. Rao, 2012.
21. M. Simonis, W. Hübner, A. Wilking, T. Huser and S. Hennig, *Scientific Reports*, 2017, **7**, 41277.
22. Z. Nan, Q. Xu, Y. Zhang and W. Ge, *IEEE Access*, 2019, **7**, 55543-55553.
23. S. S. P. Nathamgari, N. Pathak, V. Lemaitre, P. Mukherjee, J. J. Muldoon, C.-Y. Peng, T. McGuire, J. N. Leonard, J. A. Kessler and H. D. Espinosa, *Small*, 2020, **16**, 2002616.
24. G. He, J. Feng, A. Zhang, L. Zhou, R. Wen, J. Wu, C. Yang, J. Yang, C. Li, D. Chen, J. Wang, N. Hu and X. Xie, *Nano Letters*, 2019, **19**, 7201-7209.
25. Y. Cao, E. Ma, S. Cestellos-Blanco, B. Zhang, R. Qiu, Y. Su, J. A. Doudna and P. Yang, *Proceedings of the National Academy of Sciences*, 2019, **116**, 7899.
26. J. Shi, Y. Ma, J. Zhu, Y. Chen, Y. Sun, Y. Yao, Z. Yang and J. Xie, *Molecules*, 2018, **23**.

27. P. Mukherjee, S. S. P. Nathamgari, J. A. Kessler and H. D. Espinosa, *ACS Nano*, 2018, **12**, 12118-12128.
28. D. Zhao, D. Huang, Y. Li, M. Wu, W. Zhong, Q. Cheng, X. Wang, Y. Wu, X. Zhou, Z. Wei, Z. Li and Z. Liang, *Scientific Reports*, 2016, **6**, 18469.
29. Y. Li, M. Wu, D. Zhao, Z. Wei, W. Zhong, X. Wang, Z. Liang and Z. Li, *Scientific Reports*, 2015, **5**, 17817.
30. X. Xie, A. M. Xu, S. Leal-Ortiz, Y. Cao, C. C. Garner and N. A. Melosh, *ACS Nano*, 2013, **7**, 4351-4358.
31. W. Kang, F. Yavari, M. Minary-Jolandan, J. P. Giraldo-Vela, A. Safi, R. L. McNaughton, V. Parpoil and H. D. Espinosa, *Nano Letters*, 2013, **13**, 2448-2457.
32. J. E. Bestman, R. C. Ewald, S.-L. Chiu and H. T. Cline, *Nature Protocols*, 2006, **1**, 1267-1272.
33. M. L. Yarmush, A. Golberg, G. Serša, T. Kotnik and D. Miklavčič, *Annual Review of Biomedical Engineering*, 2014, **16**, 295-320.
34. M. S. Venslauskas and S. Šatkauskas, *European Biophysics Journal*, 2015, **44**, 277-289.
35. R.-C. Qian, J. Lv and Y.-T. Long, *Analytical Chemistry*, 2018, **90**, 13744-13750.
36. Y. T. Chow, S. Chen, R. Wang, C. Liu, C.-w. Kong, R. A. Li, S. H. Cheng and D. Sun, *Scientific Reports*, 2016, **6**, 24127.
37. M. Bakouei, S. Abdorahimzadeh and M. Taghipoor, *Physical Chemistry Chemical Physics*, 2020, **22**, 25306-25314.
38. Z. Orynbayeva, R. Singhal, E. A. Vitol, M. G. Schrlau, E. Papazoglou, G. Friedman and Y. Gogotsi, *Nanomedicine: Nanotechnology, Biology and Medicine*, 2012, **8**, 590-598.
39. R. Singhal, Z. Orynbayeva, R. V. Kalyana Sundaram, J. J. Niu, S. Bhattacharyya, E. A. Vitol, M. G. Schrlau, E. S. Papazoglou, G. Friedman and Y. Gogotsi, *Nature Nanotechnology*, 2011, **6**, 57-64.
40. O. Guillaume-Gentil, E. Potthoff, D. Ossola, P. Dörig, T. Zambelli and J. A. Vorholt, *Small*, 2013, **9**, 1904-1907.
41. A. Meister, M. Gabi, P. Behr, P. Studer, J. Vörös, P. Niedermann, J. Bitterli, J. Polesel-Maris, M. Liley, H. Heinzelmann and T. Zambelli, *Nano Letters*, 2009, **9**, 2501-2507.
42. P. Stiefel, F. I. Schmidt, P. Dörig, P. Behr, T. Zambelli, J. A. Vorholt and J. Mercer, *Nano Letters*, 2012, **12**, 4219-4227.
43. R. Adam Seger, P. Actis, C. Penfold, M. Maalouf, B. Vilozny and N. Pourmand, *Nanoscale*, 2012, **4**, 5843-5846.
44. J. Lv, R.-C. Qian, Y.-X. Hu, S.-C. Liu, Y. Cao, Y.-J. Zheng and Y.-T. Long, *Chemical Communications*, 2016, **52**, 13909-13911.
45. R.-J. Yu, Y.-L. Ying, R. Gao and Y.-T. Long, *Angewandte Chemie International Edition*, 2019, **58**, 3706-3714.
46. B. Babakinejad, P. Jönsson, A. López Córdoba, P. Actis, P. Novak, Y. Takahashi, A. Shevchuk, U. Anand, P. Anand, A. Drews, A. Ferrer-Montiel, D. Klenerman and Y. E. Korchev, *Analytical Chemistry*, 2013, **85**, 9333-9342.
47. F. O. Laforge, J. Carpino, S. A. Rotenberg and M. V. Mirkin, *Proceedings of the National Academy of Sciences*, 2007, **104**, 11895.
48. E. Shekaramiz, G. Varadarajalu, P. J. Day and H. K. Wickramasinghe, *Scientific Reports*, 2016, **6**, 29051.
49. A. P. Ivanov, P. Actis, P. Jönsson, D. Klenerman, Y. Korchev and J. B. Edel, *ACS Nano*, 2015, **9**, 3587-3595.
50. N. Varongchayakul, J. Song, A. Meller and M. W. Grinstaff, *Chemical Society Reviews*, 2018, **47**, 8512-8524.
51. V. Kurz, T. Tanaka and G. Timp, *Nano Letters*, 2014, **14**, 604-611.
52. J.-A. Huang, V. Caprettini, Y. Zhao, G. Melle, N. Maccaferri, L. Deleye, X. Zambrana-Puyalto, M. Ardini, F. Tantussi, M. Dipalo and F. De Angelis, *Nano Letters*, 2019, **19**, 722-731.
53. N. Panday, G. Qian, X. Wang, S. Chang, P. Pandey and J. He, *ACS Nano*, 2016, **10**, 11237-11248.
54. C. C. Chau, S. E. Radford, E. W. Hewitt and P. Actis, *Nano Letters*, 2020, **20**, 5553-5561.
55. C. C. Chau, E. W. Hewitt and P. Actis, *Current Opinion in Electrochemistry*, 2021, **25**, 100654.
56. Y. Liu, M. K. Shipton, J. Ryan, E. D. Kaufman, S. Franzen and D. L. Feldheim, *Analytical Chemistry*, 2007, **79**, 2221-2229.
57. A. S. Rubfiaro, P. S. Tsegay, Y. Lai, E. Cabello, M. Shaver, J. Hutcheson, Y. Liu and J. He, *ACS Applied Bio Materials*, 2021, **4**, 1632-1639.
58. X. Lian, J. Zhang, S. M. Azarin, K. Zhu, L. B. Hazeltine, X. Bao, C. Hsiao, T. J. Kamp and S. P. Palecek, *Nature Protocols*, 2013, **8**, 162-175.
59. S. Tohyama, F. Hattori, M. Sano, T. Hishiki, Y. Nagahata, T. Matsuura, H. Hashimoto, T. Suzuki, H. Yamashita, Y. Satoh, T. Egashira, T. Seki, N. Muraoka, H. Yamakawa, Y. Ohgino, T. Tanaka, M. Yoichi, S. Yuasa, M. Murata, M. Suematsu and K. Fukuda, *Cell Stem Cell*, 2013, **12**, 127-137.
60. W. Strober, *Current Protocols in Immunology*, 1997, **21**, A.3B.1-A.3B.2.
61. J. Guo, A. Sesena Rubfiaro, Y. Lai, J. Moscoso, F. Chen, Y. Liu, X. Wang and J. He, *Analyst*, 2020, **145**, 4852-4859.
62. P. Pandey, N. Panday, S. Chang, P. Pang, J. Garcia, X. Wang, Q. Fu and J. He, *ChemElectroChem*, 2018, **5**, 3102-3112.
63. L. Yin, W. Wang, S. Wang, F. Zhang, S. Zhang and N. Tao, *Biosensors & bioelectronics*, 2015, **66**, 412-416.